ORIGINAL ARTICLE

Superior photocatalytic activity of tungsten disulfide nanostructures: role of morphology and defects

Waseem Ashraf[1] · Tarab Fatima[1] · Ketki Srivastava[1] · Manika Khanuja[1]

Abstract

Tungsten disulphide (WS_2) nanostructures, WS_2 nanosheets (W_{NS}) and WS_2 nanorods (W_{NR}), were synthesized by varying the surfactant, *N*-cetyl-*N, N,N*-trimethyl ammonium bromide (CTAB), concentration using facile hydrothermal technique. Samples were characterized by high-resolution transmission electron microscopy (HRTEM) and field emission scanning electron microscopy (FESEM) for morphology, X-ray diffraction (XRD) to confirm their phase and crystal structure, photoluminescence (PL) and Raman studies for the determination of defect density, Tauc plot for the determination of band gap, Fourier transform infra red (FTIR) spectroscopy for functional groups and bonds, and Brunauer–Emmett–Teller (BET) isotherms for the determination of pore size and surface area. A comparative study using WS_2 nanostructures (W_{NS} and W_{NR}) was conducted to observe the photocatalytic degradation efficiency (η) and degradation kinetics on methylene blue (MB) and 4-chlorophenol (4-CP). The superior photocatalytic performance of W_{NS} over W_{NR} is attributed to enhanced pore size and reduced defect density. High-performance liquid chromatography was carried out for the determination of intermediate products during photocatalytic degradation.

Keywords WS_2 nanostructures · Photocatalysis · High-performance liquid chromatography · Photoluminescence · Raman

Introduction

Due to widespread industrialization, an increase in the level of contaminants in water bodies such as organic pollutants, dyes and other toxic chemicals has been reported. These chemical effluents accumulate in water bodies and cause severe harm to the ecosystem as well as living beings (Bhuyan et al. 2015a). Reported by a global survey, potable water will be reduced to 15% in the next 15 years. The problem of water pollution exists worldwide and there is a dire need to remove the pollutants from water bodies using new scientific technological advancements (Singh et al. 2017a). 4-chlorophenol (4-CP) is a commonly found non-biodegradable and toxic pollutant generated as a chemical waste from agrochemical, paper and pharmaceutical industries (Kartal and Sökmen 2011; Rideh et al. 1997). Its consumption, when greater than 0.1 mg/ml can be hazardous to living beings (Aslam et al. 2015). Similarly, methylene blue (MB),

a cationic dye, is widely used in the paper and textile industries; however, it has many drawbacks to its usage. Not only does this dye cause water pollution but also when consumed by living beings can be a major cause of increased heart rate, jaundice and tissue necrosis (Khodaie et al. 2013). Several methods have been adopted for the removal of these industrial pollutants from water bodies, such as adsorption, enzymatic decomposition and microbial decomposition (Nguyen and Juang 2015; Yue et al. 2002; Theurich et al. 1996). It has been reported that photocatalysis is an effective method for the removal of wide range of pollutants. It uses solar energy ($h\nu$) as a source to form radicals that oxidize these pollutants and cause their catalytic degradation (Singh et al. 2018).

In the present case scenario, a lot of research has been conducted on the photocatalytic activity of various nanostructures. Metal oxide semiconductors such as TiO_2 and ZnO are the most commonly studied photocatalysts; however, their wide bandgap limits their applications within the UV range and allows them to capture only 5% of the total sunlight (Sharma et al. 2017a, b). The energy conversion efficiency of nanostructured materials can be enhanced by reducing the number of defects (Zhang et al. 2015a, b). For example, monocrystalline silicon provides the highest efficiency in all available

✉ Manika Khanuja
  manikakhanuja@gmail.com

1 Centre for Nanoscience and Nanotechnology, Jamia Millia Islamia, New Delhi 110025, India

Springer

PV modules due to the presence of ultra-low defects (Wang et al. 2018). To reduce the defect layer thickness, nano-twinned surfaces (Zhang et al. 2016a, b), self-matching of stack faults (Zhang et al. 2018), mechanical chemical grinding (Zhang et al. 2017a), nanogrinding (Yu et al. 2013), very thin abrasives and fundamental mechanism underlying the abrasive machining are reported and used in wafering of solar cells; novel approach of scratching at m/s and nanoscale is proposed and to control the defects, a new tetragonal phase of Si is discovered (Zhang et al. 2012, 2016a, b, 2017b, c; Guo et al. 2018).

Many nanocomposite photocatalysts have been developed to enhance the visible light-driven photocatalytic activity with reduced electron–hole recombination, yet it remains a challenge to attain very high efficiency with less complexity (Bhuyan et al. 2015a, b; Sharma et al. 2016). Recently, the equation has shifted towards 2D transition metal disulfides (TMDs) that consist of S–M–S layers connected via strong intramolecular bonds but weak interlayer interaction due to van der Waals forces. They have caught considerable attention in several applications such as photocatalysis, biosensors, drug delivery, and electronic devices due to their unique electrical, mechanical and optical properties (Siddiqui et al. 2018; Singhal et al. 2018; Narang et al. 2018; Liu and Liu 2017; Chaudhary et al. 2018). Among all the TMDs, WS_2 can be considered as the promising material for photocatalysis due to (1) wide spectral range, from NIR to UV, (2) biocompatibility, (3) high biodegradability, (4) strong W–S bond, (5) tunable morphology and (6) ease of synthesis (Peng et al. 2017; Sade and Lellouche 2018; Goldman et al. 2015; Vattikuti et al. 2016a, b). WS_2 nanomaterials have been synthesized by several methods such as CVD, thermal decomposition, laser ablation, exfoliation and sputtering; however, these methods require high temperature and harsh conditions which limits their applications (Wu et al. 2017; Tang et al. 2011). Hydrothermal synthesis, on the other hand, has been reported as an effective environment-friendly technique for the fabrication of various nanostructures owing to its advantages of low temperature, large-scale production and facile synthesis (Narang et al. 2017; Cao et al. 2015). In this work, we report the hydrothermal synthesis of two different morphologies of WS_2 nanostructures, WS_2 nanosheets (W_{NS}) and WS_2 nanorods (W_{NR}), by varying the surfactant (CTAB) concentration. A systematic comparative study is carried out to analyze the photocatalytic behavior of WS_2 nanostructures on 4-CP and MB. A detailed study on intermediate products formed during degradation is carried out through HPLC.

Experimental
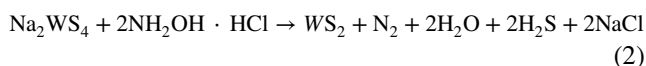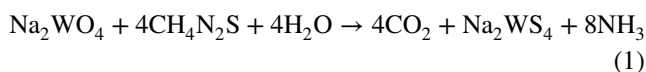
Materials

Sodium tungstate dihydrate (Mw 329.86 g/mol, assay 96%) and thiourea (Mw 76.12 g/mol, assay 99.0–101.0%) were purchased from Thermo Fisher Scientific India Pvt. Ltd., Mumbai, India. Hydroxylamine hydrochloride (Mw 69.49 g/mol, assay 98%), CTAB (Mw 364.45 g/mol, assay 98%) and polyethylene glycol (PEG) 4000 flakes/powder (average Mw 3500–4500 g/mol) were purchased from Central Drug House (P) Ltd., New Delhi, India. MB (Mw 319.85 g/mol, assay 96%) and 4-chlorophenol (Mw 128.56 g/mol, assay 99%) were purchased from Thermo Fisher Scientific India Pvt. Ltd., Mumbai, India. TiO_2 (Aeroxide®, P25 nanoparticles, Acros Organics) was used as the reference photocatalytic material.

Method of synthesis

For nanosheets, 0.005 mol of sodium tungstate ($Na_2WO_4 \cdot 2H_2O$) was mixed with 0.02 mol of thiourea (CH_4N_2S) and 0.01 mol of hydroxylamine hydrochloride ($NH_2OH \cdot HCl$) in 30 ml of DI water under constant stirring. To this solution, 0.24 g of surfactant (CTAB) was added and the solution was stirred for an hour. A white color precipitate was formed and the pH of the solution was observed to be 6.15. The contents were transferred to a 50-ml teflon-lined autoclave and placed in the reaction furnace at 180 °C for 24 h. The autoclave was allowed to cool down under natural conditions till room temperature. The contents of the autoclave were subjected to filtration process where they were washed with DI water and ethanol and finally allowed to dry at 30 °C for 4 h. Similarly, for the synthesis of WS_2 nanorods, 0.18 g of surfactant (CTAB) was used and pH of 7.25 was observed.

The reactions for the synthesis are as follows:

$$Na_2WO_4 + 4CH_4N_2S + 4H_2O \rightarrow 4CO_2 + Na_2WS_4 + 8NH_3 \tag{1}$$

$$Na_2WS_4 + 2NH_2OH \cdot HCl \rightarrow WS_2 + N_2 + 2H_2O + 2H_2S + 2NaCl \tag{2}$$

Characterization of samples

The morphology of the catalysts was studied by high-resolution transmission electron microscopy (HRTEM Techno, FEI) and field emission scanning electron microscopy (FESEM Zeiss, Sigma). Phase identification was observed by X-ray diffraction (XRD Smart Lab Guidance, Rigaku) using Cu K_α X-ray radiation ($\lambda = 1.5418$ Å). UV–Vis spectroscopy (UV–Vis Cary Series, Agilent

Technologies) was performed to observe the photocatalytic activity of the WS$_2$ nanostructures against MB and 4-CP. Functional groups and bonds were detected by FTIR (Vertex 70V, Bruker) spectroscopy. The surface area and pore size distribution of WS$_2$ nanostructures were determined experimentally by Brunauer–Emmett–Teller (BET) and Barrett–Joyner–Halenda (BJH) analyses. Nitrogen adsorption–desorption isotherms were measured at 77.4 K using (NOVA-1000 version 370). The photoluminescence emission spectra were recorded at room temperature using a spectro-fluorometer (Edinburgh instruments-FLS 980) at excitation wavelength of 325 nm with a scan range of 350–800 nm. The intermediate degradation products of 4-CP were determined by HPLC-Agilent Technologies (1260 ∞ series) Hi-Plex X column with DI water as mobile phase and a detector temperature of 35 °C and column temperature of 65 °C along with a pump flow rate of 0.6 ml/min.

Procedure for photocatalysis

A comparative study was conducted to study the photodegradation behavior of WS$_2$ nanostructures against MB and 4-CP. A solution of 1 mg/100 ml each was prepared and stirred in dark for half an hour. To this, WS$_2$ photocatalyst was added and stirred. A dark blue solution was formed which was illuminated using an AM 1.5 solar illumination of 100 mW/cm^2 from xenon arc lamp in ambient atmosphere. 1 ml solution was taken out at intervals of 10 min for 1 h with the initial sample taken at 0 min. Two such studies

were conducted, one with 50 mg of photocatalyst and the other with 20 mg of photocatalyst. The collected samples were centrifuged and the supernatant was separated. The UV–Vis spectra of supernatant were taken using DI water as reference. To further explore the photocatalytic activity of WS$_2$ nanostructures, 4-CP was selected as the model organic pollutant. An aqueous solution of 0.5 mg/100 ml was prepared to which 50 mg of the photocatalyst was added. 1 ml of solution was taken out at intervals of 30 min for 2 h and the samples obtained were analyzed using UV–Vis spectroscopy. Time-dependent UV–Vis spectroscopy was also carried out on MB and 4-CP without photocatalyst and with commercially available TiO$_2$ nanoparticles (Aeroxide®, P25 nanoparticles, Acros Organics) as the reference material (Fig. 1).

Results and discussion

Figure 2a, b shows the HRTEM micrographs of W$_{NS}$ and W$_{NR}$ (Fig. 2b insert shows magnified image of WS$_2$ nanorods). Thus, clear change in morphology from nanosheets to nanorods with surfactant concentration is evidenced from TEM micrographs.

The FESEM was used to verify the morphology of WS$_2$ nanostructures. Figure 3a exhibits the sheet-like structure of WS$_2$ nanostructures (W$_{NS}$) with average length ~ 600 nm and width ~ 350 nm. Figure 3b exhibits the rod-like structure of WS$_2$ nanostructures (W$_{NR}$). The average dimensions
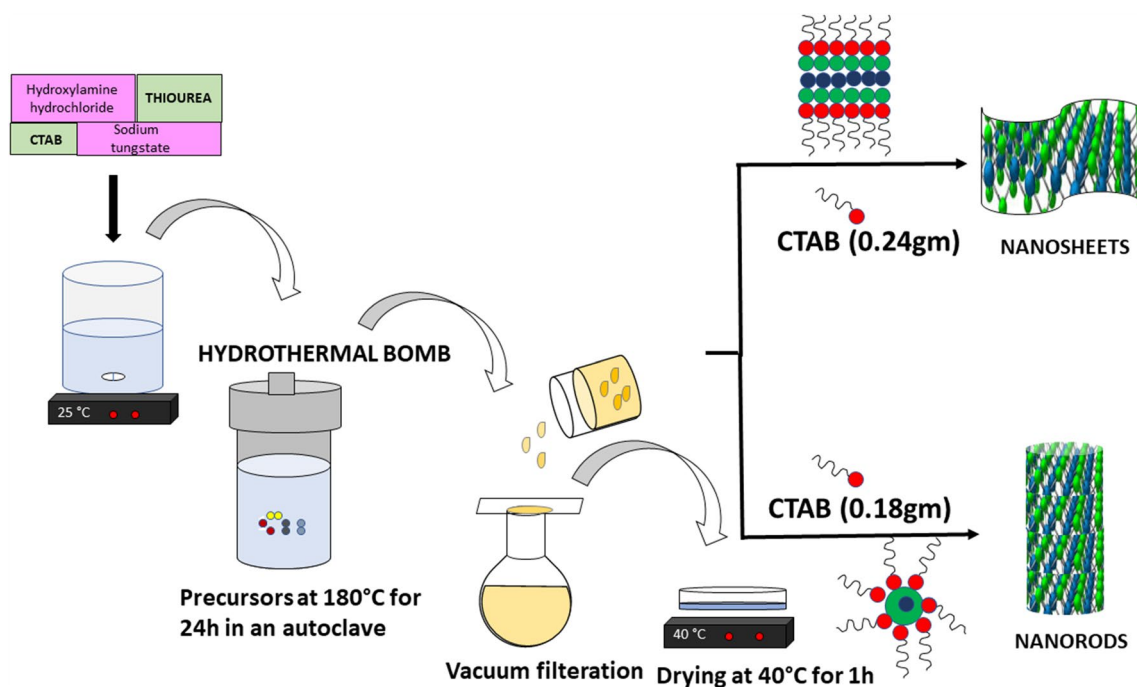
Fig. 1 Schematic representation of hydrothermal synthesis of WS$_2$ nanostructures: WS$_2$ nanosheets (W$_{NS}$) and WS$_2$ nanorods (W$_{NR}$)

Fig. 2 HRTEM micrographs of **a** W_{NS} and **b** W_{NR} (insert shows the magnified image of W_{NR})
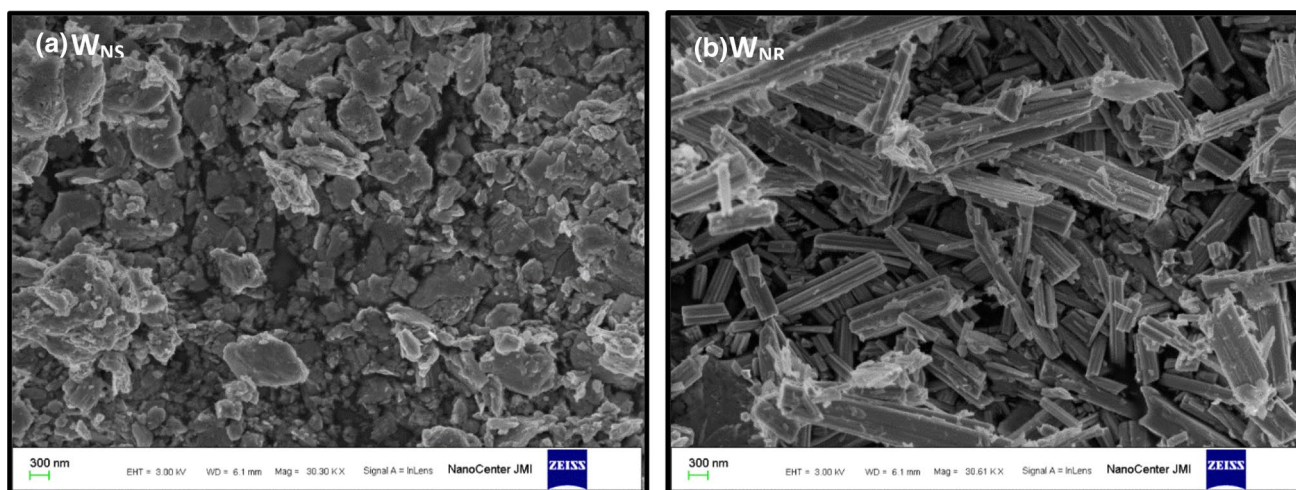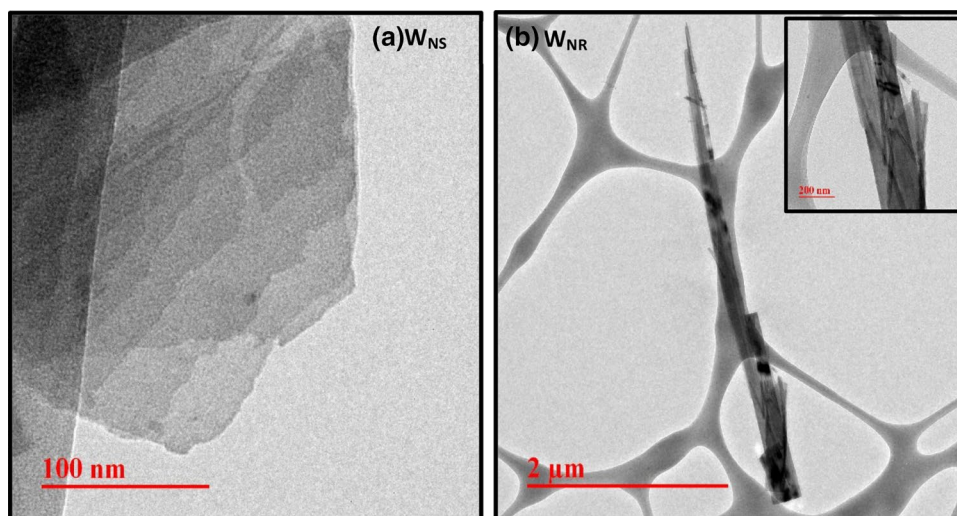
Fig. 3 FESEM micrographs of **a** W_{NS} and **b** W_{NR}

of the nanorods are; length ~ 500 nm and diameter ~ 100 to 150 nm. Thus, FESEM study confirms that synthesized WS_2 nanostructures possess sheet- and rod-like morphology in accordance with the TEM results (Fig. 2).

Synthesis mechanism of WS_2 nanostructures

During the synthesis of WS_2 nanostructures, addition of hydroxylamine hydrochloride ($NH_2OH \cdot HCl$) to the mixture of sodium tungstate ($Na_2WO_4 \cdot 2H_2O$) and thiourea (CH_4N_2S) acts as a reducing agent, thereby causing the initiation of nucleation process. The nucleus then undergoes Ostwald ripening and it grows due to the assembly of other nuclei. The formed nuclei assemble in order to reduce high surface energy. Surfactant (CTAB) plays a crucial role in the formation of different morphologies of WS_2 nanostructures

formed due to its influence on interface energy and orientation. When the concentration of CTAB was 0.18 g, the obtained WS_2 nanostructures were rod shaped. However, when the CTAB concentration was increased to 0.24 g, the synthesized WS_2 nanostructures possess sheet-like morphology. In the case of nanorods, the CTAB molecules orient themselves in such a way that the hydrophobic tail points away from the micelle while the surfactant heads influence the particles of WS_4^{2-} ions to form nanorods by subsequent crystal growth. This is also supported by the interaction of CTA^+ and WS_4^{2-} ions. As soon as the concentration of surfactant comes up to a critical micelle concentration (CMC), the surfactant molecules align themselves in a lamellar orientation to keep the energy of the system low. Thus, in the present study, critical micellar concentration leads to the formation of WS_2 nanosheets. The addition of a surfactant
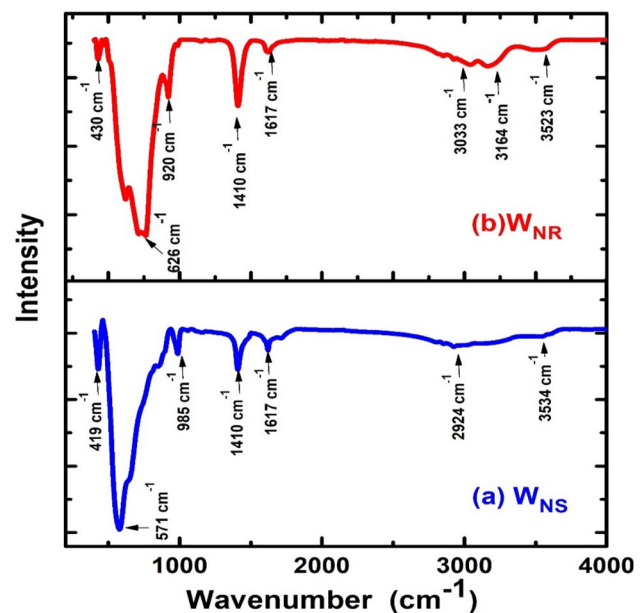
Table 1 Properties of hydrothermally synthesized WS_2 nanostructures as a function of synthesis parameters

S. No.	Morphology	Temperature (°C)	Time (h)	References
1	Hexagonal WS_2 platelets	150	12	Vattikuti et al. (2016b)
2	Mesoporous WS_2 nanosheets	180	6	Vattikuti et al. (2016a)
3	WS_2 nanosheets	220	48	Piao et al. (2018)
4	WS_2 nanorods	180	24	Tang et al. (2011)
5	WS_2 nanosheets, nanorods, nanofibers	180	24	Cao et al. (2014)
6	WS_2 nanosheets	265	24	Navale et al. (2015)
7	Hyacinth flower-like WS_2 nanorods	200	24	Wu et al. (2017)
8	WS_2 nanosheets and nanorods	180	24	Present work
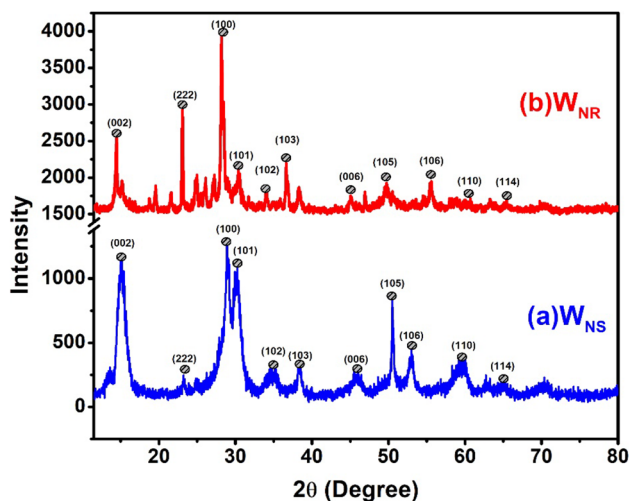
Fig. 4 XRD diffractogram of **a** W_{NS} and **b** W_{NR}

Fig. 5 FTIR spectra of **a** W_{NS} and **b** W_{NR}

allows the crystal growth to occur in a three-dimensional assembly due to van der Waals forces (Cao et al. 2014; Tang et al. 2011). In addition to the surfactant concentration, the morphology of the WS_2 nanostructures also depends on different synthesis parameters such as temperature and time as shown in Table 1.

To determine the crystal structure of WS_2 nanostructures, XRD study was carried out as shown in Fig. 4a, b. The peaks were observed at 2θ (hkl): 14.39° (002), 23.09° (222), 28.15° (100), 30.22 (101), 34.8° (102), 38.32° (103), 44.94° (006) 50.61° (105), 55.4 (106), 59.4° (110) and 65.27° (114) for synthesized WS_2 nanostructures (JCPDS no: 87-2417 and 84-1398); however, there is a shift obtained in the peak positions of (103), (106). The peak at (222) is attributed to the presence of sulfur. A strong (002) peak indicates the highly ordered stacking of WS_2 nanostructures. The difference in the intensities of the peaks observed for hkl planes (105) and (101) may be attributed to the difference in the morphology of the WS_2 nanostructures. As evident from Fig. 4, the number of peaks in the XRD for W_{NR} is more than that for W_{NS}. This indicates that the W_{NR} possess more polycrystalline

character and hence higher number of grain boundaries than W_{NS}. The increase in the number of grain boundaries leads to higher dislocation density and hence more structural disorders (Vattikuti et al. 2016a, b).

The synthesis of WS_2 nanostructures was confirmed using FTIR spectroscopy as shown in Fig. 5a, b. The bands at 571 cm^{-1} and 626 cm^{-1} are attributed to W–S bonds, while 985 cm^{-1} and 920 cm^{-1} corresponded to S–S bonds in W_{NS} and W_{NR}, respectively. The bands obtained at 1410 cm^{-1} and 1617 cm^{-1} are both attributed to stretching deformation of hydroxyl group. The small peaks obtained at 2924 cm^{-1} and 3534 cm^{-1} for W_{NS} and 3033 cm^{-1}, 3164 cm^{-1} and 3523 cm^{-1} for W_{NR} corresponded to OH vibration (Vattikuti et al. 2016b).

The bandgaps of the WS_2 nanostructures W_{NS} and W_{NR} are shown in Fig. 6a and b, respectively. A graph is plotted between $(\alpha h\upsilon)^{1/2}$ and $h\upsilon$, where α is the absorption coefficient, defined as $\alpha = 2.303$ A/t, where 'A' is the
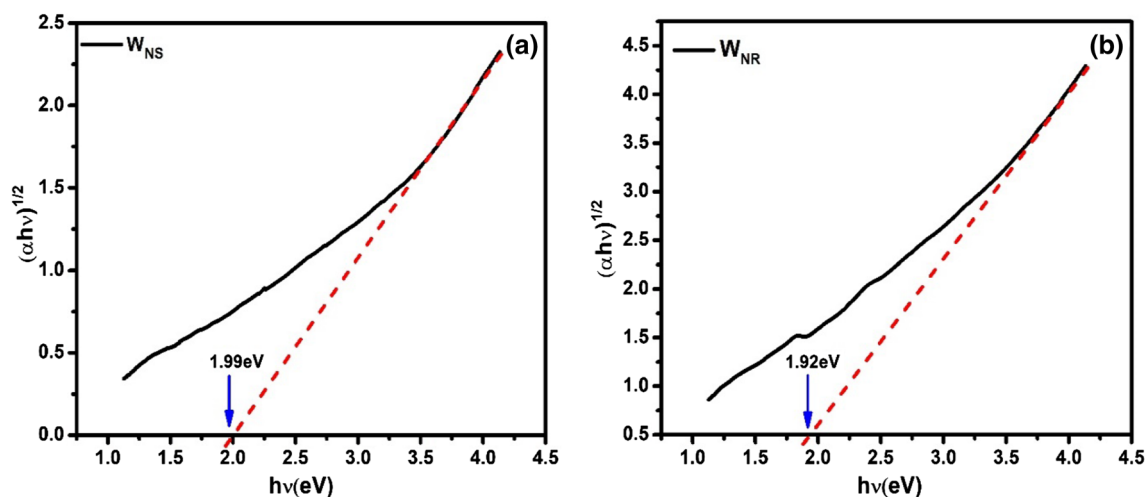
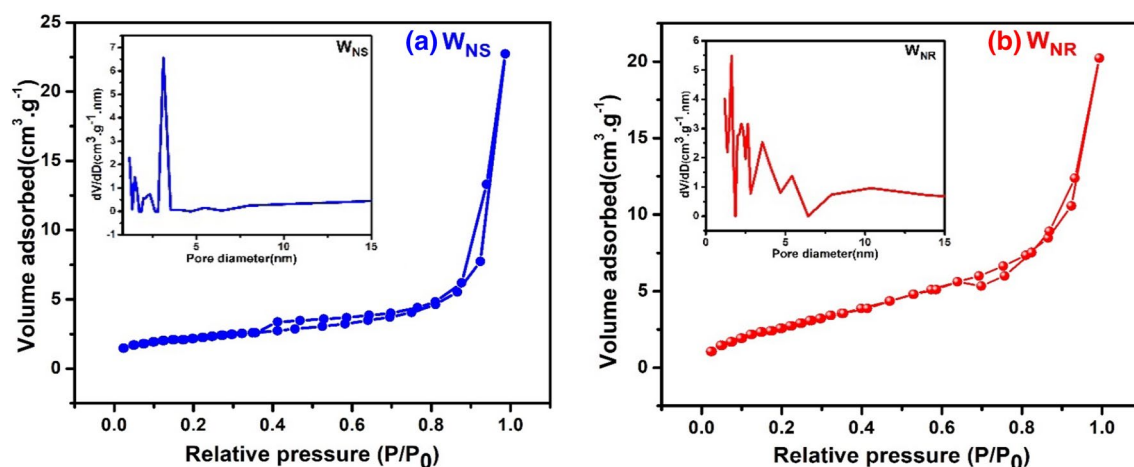**Fig. 6** Tauc plot of **a** W_{NS} and **b** W_{NR}

Fig. 7 N2 adsorption–desorption isotherm of **a** W_{NS} and **b** W_{NR} with Barrette–Joynere–Halenda (BJH) pore size distribution in the insert

absorbance and 't' is the thickness of the cuvette. A tangent is drawn on the graph to get the energy value of bandgap. The estimated bandgap is 1.99 eV and 1.92 eV for W_{NS} and W_{NR}, respectively.

The Brunauer–Emmett–Teller analysis was used to determine the surface area of the photocatalysts W_{NS} and W_{NR} by adsorption and desorption isotherms using nitrogen as an analysis gas. 0.03 g of each catalyst in the powder form was taken and degassed at 150 °C for 12 h under vacuum before each measurement. The catalysts were then subjected to outgassing for 1 h at 100 °C. The nitrogen adsorption–desorption isotherms obtained for W_{NS} and W_{NR} (Fig. 7a, b) were found to be of TYPE H4 according to BET classification which forms a convex to the x-axis over its entire range with hysteresis observed which usually occurs in the case of mesoporous structures. The pore diameters of 3.118 nm

Table 2 BET analysis of W_{NS} and W_{NR}

Sample	Pore volume (cc/g)	Pore diameter (nm)	Surface area (g/m^2)
W_{NS}	0.021	3.118	7.541
W_{NR}	0.023	1.614	10.855

and 1.614 nm for W_{NS} and W_{NR} suggest that the material is mesoporous (2 nm < size < 50 nm) (Leofanti et al. 1998) (Table 2).

A negligible change in the surface area of the catalysts is seen when morphology is changed suggesting that the surface area may not be the key factor responsible for the higher catalytic activity of W_{NS} over W_{NR}. In this case, a

larger pore size of W_{NS} is responsible for its higher photocatalytic activity as compared to W_{NR}. The larger pore size enhances the probability of active sites responsible for slowing down the recombination process thereby causing more holes and electrons to react with the substrate molecules that are adsorbed on the surface, which in this case are MB and 4-CP, at a faster rate. This confirms that W_{NS} shows greater photocatalytic degradation over W_{NR} (Moonsiri et al. 2004; He et al. 2015).

The photoluminescence plots of W_{NS} and W_{NR} are shown in Fig. 8a and b, respectively. Two major kinds of peaks, near-band edge (NBE) emission band or UV band and broad visible emission band also known as the defect level (DL) band, were observed. The peaks are obtained at 3.07 eV (403 nm), 2.89 eV (429 nm) and 1.907 eV (650 nm) for W_{NS} and at 3.26 eV (380 nm), 2.98 eV (415 nm) and 1.94 eV (636 nm) for W_{NR}, respectively. The peaks observed at 1.907 eV (650 nm) and 1.94 eV (636 nm) are ascribed to the direct band edge transition from conduction band minima to valence band maxima. The peaks at 2.89 eV (429 nm) and 2.98 eV (415 nm) in W_{NS} and W_{NR}, respectively, are attributed to quantum-confined transition while the peaks observed at 3.07 eV (403 nm) and 3.26 eV (380 nm) for W_{NS} and W_{NR}, respectively, may be due to the defect state transition (Ghorai et al. 2016, 2017). A lower intensity is observed for W_{NR} which is due the excess defects present in the sample. As the number of defects increases, the PL intensity decreases as these defects act as non-radiative recombination trapping centres. They lead to an increase in electron–hole recombination rate (Sharma et al. 2017a, b; Baral et al. 2017).

Figure 9 shows the Raman spectra of W_{NS} and W_{NR}, which depict two active modes E_{2g}^{1} and A_{1g}, the A_{1g} mode assigned to the S atoms which are moving in-phase and in out-of-plane directions while E_{2g}^{1} mode arises from in-phase
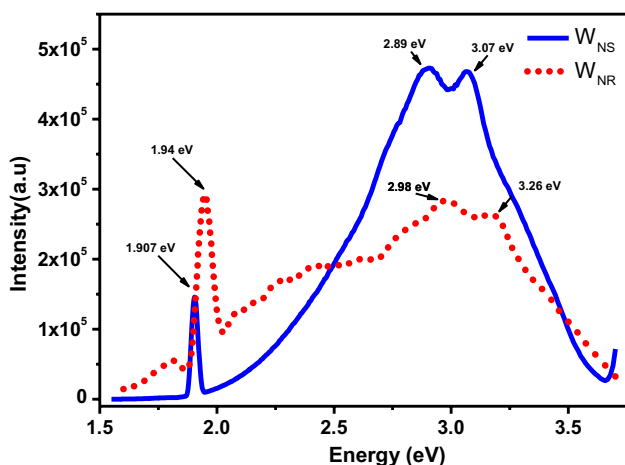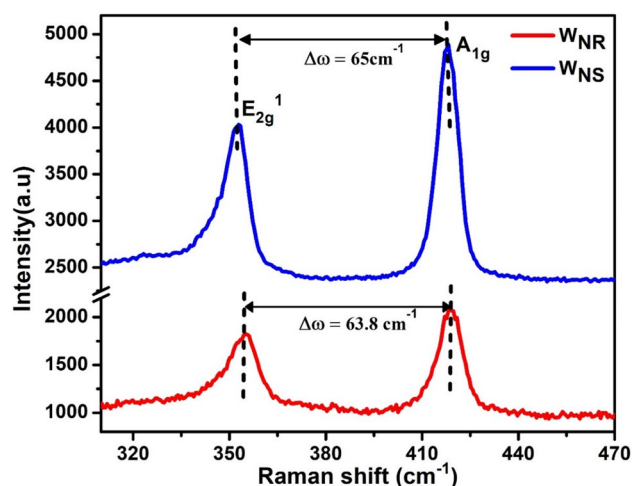

Fig. 9 Raman spectra of W_{NS} and W_{NR} obtained at laser excitation of 514 nm

vibrations of W atoms vibrating in-phase in the opposite direction with respect to S atoms. In case of W_{NS}, peaks were observed at E_{2g}^{1} mode at 353 cm^{-1} and A_{1g} mode at 418 cm^{-1}, whereas in W_{NR}, E_{2g}^{1} mode at 354.9 cm^{-1} and A_{1g} mode at 418.7 cm^{-1}. The '$\Delta\omega$' values between E_{2g}^{1} and A_{1g} modes are 65 cm^{-1} and 63.8 cm^{-1} for W_{NS} and W_{NR}, respectively.

FWHM is 12.95 cm^{-1} (E_{2g}^{1}) and 9.808 cm^{-1} (A_{1g}) for W_{NR} and 10.82 cm^{-1} (E_{2g}^{1}) and 8.2 cm^{-1} (A_{1g}) for W_{NS} which indicates peak broadening in case of W_{NR}, and the decrease in intensity of W_{NR} with respect to W_{NS} implied more defects in W_{NR} as compared to W_{NS} (Shi et al. 2016).

Photocatalytic activity

A comparative study was conducted to test the photocatalytic activity of WS_2 nanostructures against MB and 4-CP. The degradation of organic pollutant was studied as a function of time.

To study the photocatalytic degradation mechanism, first, the dark reaction (wherein the light source was removed) was carried out using MB aqueous dye solution, and W_{NS} and W_{NR} catalysts were allowed to react with the dye in dark conditions as shown in Fig. 10a and b, respectively. UV–Vis absorption spectra were recorded for time ($t = 0$ min and 20 min) for both W_{NS} and W_{NR} (Fig. 10). As evident from the figure, no change in the intensity was observed even after 20 min thereby confirming that no degradation of dyes has taken place in dark due to surface adsorption phenomenon.

Figure 11a, b depicts the photocatalytic degradation of MB using 50 mg of W_{NS} and W_{NR}, respectively. The samples were collected at times $t = 0$, 15, 30, 45 and 60 min to study the time-dependent photocatalytic MB degradation. Figure 11c shows a plot of relative absorbance (C/C_0) vs
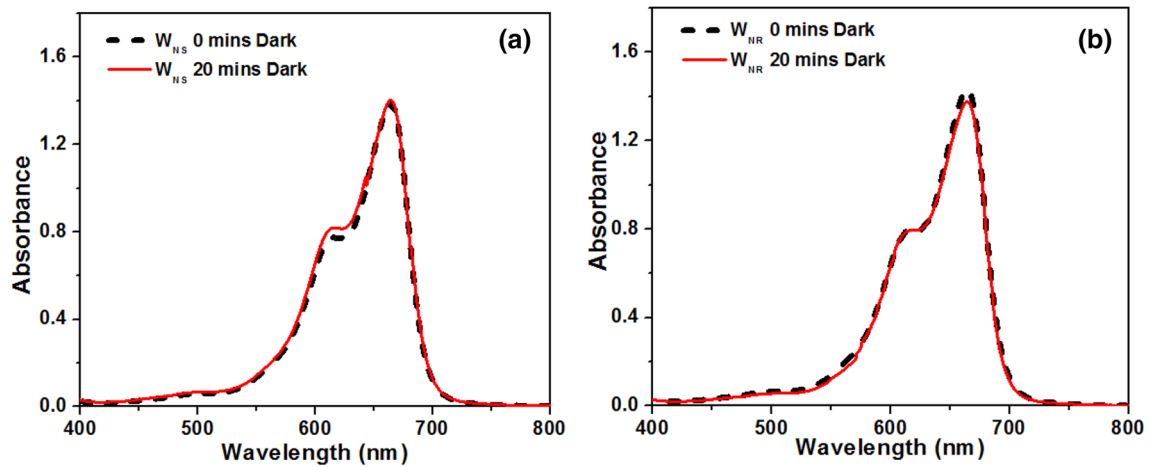

Fig. 8 Photoluminescence (PL) spectra of W_{NS} and W_{NR}

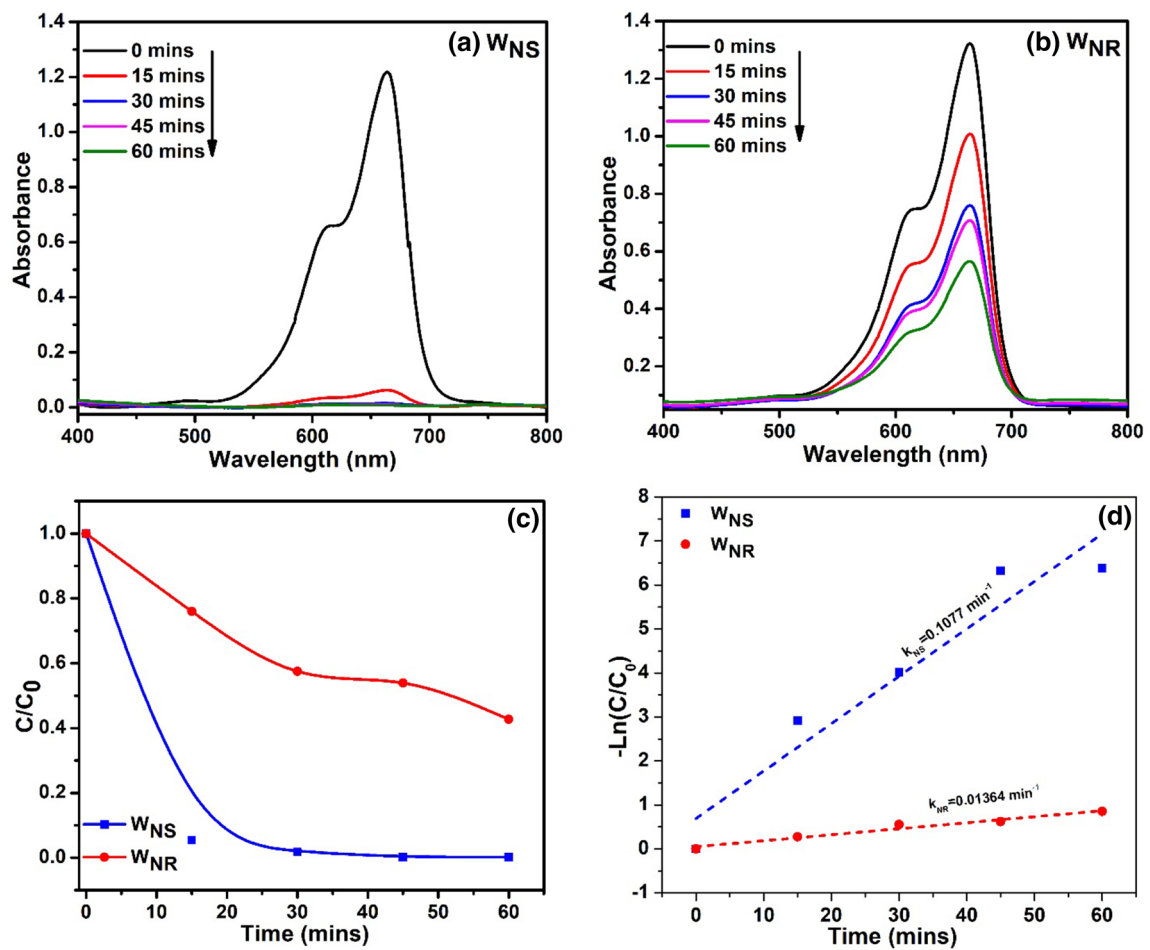**Fig. 10** MB dark reaction with **a** W_{NS} and **b** W_{NR}

Fig. 11 Time-dependent UV–Vis spectra of MB dye using 50 mg of **a** W_{NS}, **b** W_{NR} and respective **c** C/C_0 vs time plot and **d** $-\ln (C/C_0)$ vs time plot

time. It is observed that W_{NS} are more efficient in photo-degradation of the dye solution as compared to W_{NR}. C/C_0 is the ratio of intensity at time 't' and intensity at time 't_0'. Photocatalytic degradation follows the first-order rate kinetics, described by the following equation:

$$C = C_0 e^{-kt}$$
$$\Rightarrow -\ln(C/C_0) = kt \tag{3}$$

where k gives the rate constant of the reaction, 'C' is the intensity of absorbance at time 't', 'C_0' is the initial intensity of absorbance at 0 min and 't' is the time. The rate constant of the reaction is calculated by plotting a graph between $-\ln(C/C_0)$ and time and the corresponding slope was determined. The rate constants were found to be 0.1077 min^{-1} for W_{NS} and 0.01364 for W_{NR} min^{-1} for 50 mg of the photocatalyst as shown in Fig. 11d. As evident from Fig. 11, ~95% of the dye was degraded in the first 15 min using W_{NS} and the rate constant was also observed to be ten times higher than that of W_{NR}. Time-dependent photocatalytic study was

also carried out using lower concentration (20 mg) of the photocatalyst to study the catalyst efficiency.

Figure 12a, b shows time-dependent UV–Vis spectra of MB using 20 mg W_{NS} and W_{NR}. The aforementioned experiment was also repeated using commercially available TiO$_2$ nanoparticles (as reference) and without catalyst too. A sharp decrease in the intensity of MB peak is observed for catalyst W_{NS} as compared to W_{NR}. Figure 12c shows a plot of relative absorbance (C/C_0) vs time for W_{NS}, W_{NR}, TiO$_2$ and without photocatalyst. No significant decrease was observed without photocatalyst. The maximum photocatalytic activity was shown by W_{NS} followed by TiO$_2$ and then W_{NR}. Figure 12d shows the rate constant (k) of 0.09106 min^{-1} for W_{NS}, 0.02334 min^{-1} for TiO$_2$, 0.00958 min^{-1} for W_{NR} and 0.00201 min^{-1} without photocatalyst. The rate constant of W_{NS} was found to be ~ 10 times that of W_{NR} in both the studies using 20 mg and 50 mg of respective photocatalysts. It is quite evident that higher the rate constant, better the degradation of pollutant. Thus, from the above data, it can be concluded
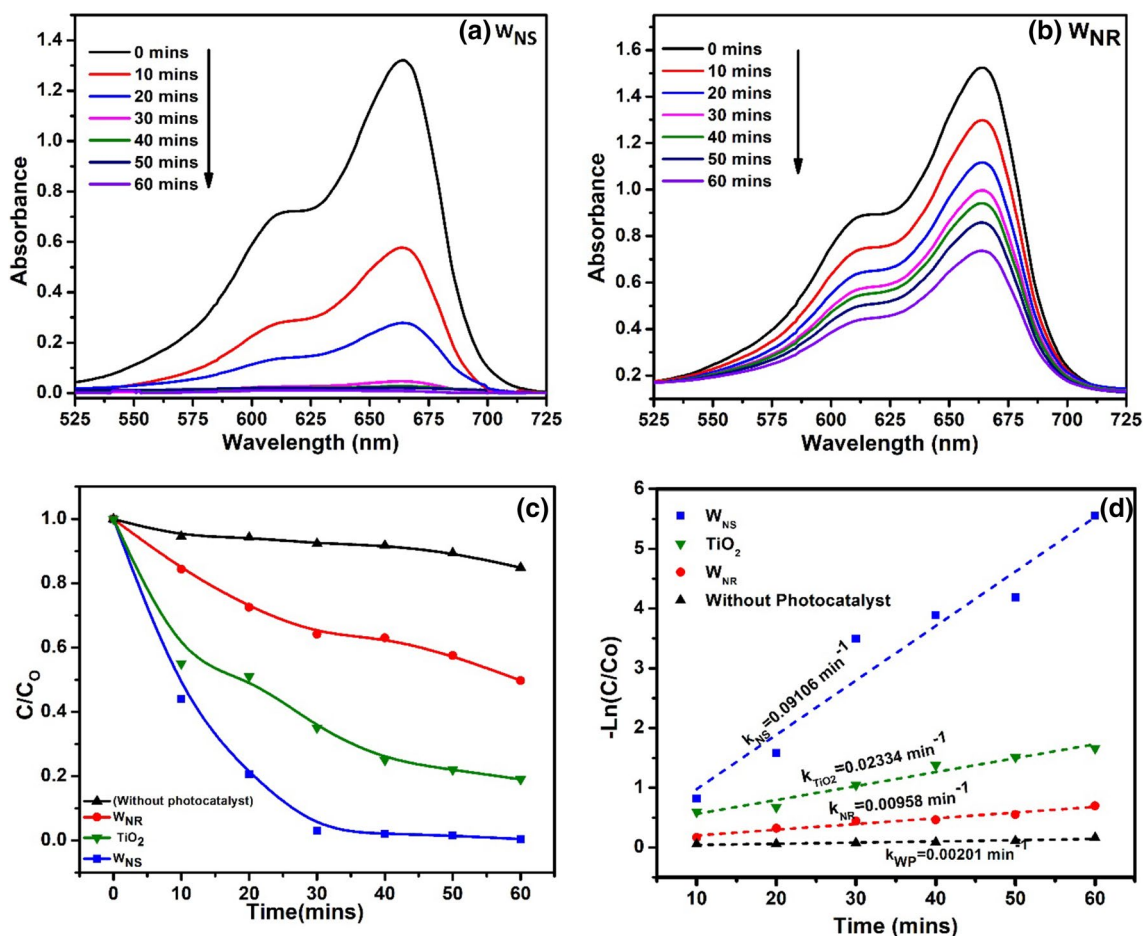
Fig. 12 Time-dependent UV–Vis spectra of MB dye using 20 mg of **a** W_{NS}, **b** W_{NR}, **c** C/C_0 vs time plot and **d** photodegradation kinetics of MB catalyzed by W_{NS}, W_{NR}, TiO$_2$ and without photocatalyst

that W_{NS} has a higher photocatalytic degradation rate as compared to others.

The photodegradation efficiency was calculated using the following formula:

$$\eta = \{1 - [C/C_0]\} \times 100\% \qquad (4)$$

where η is efficiency, C is the intensity at a time 't' and C_0 is the intensity at time 't$_0$'.

As shown in Fig. 13a, b, the photodegradation efficiencies obtained using 50 mg of MB photocatalyst at times $t = 15, 30, 45$ and 60 min are 94.6%, 98.2%, 99.82%, and 99.83% for W_{NS} and 24%, 42.5%, 46.1% and 57.3% for W_{NR}, respectively. Similarly, the efficiencies obtained using 20 mg of the WS_2 photocatalyst at times $t = 10, 20, 30, 40, 50$ and 60 min are 55.9%, 79.4%, 96.9%, 97.9%, 98.4%, 99.6% for W_{NS} and 15.6%, 27.47%, 35.81%, 36.97%, 42.44% and 50.23% for W_{NR}, respectively.

A similar study was conducted to study the degradation of 4-CP using W_{NS} and W_{NR}. UV–Vis absorption spectra were recorded for times $t = 0$ min and 20 min for both W_{NS} and W_{NR} as shown in Fig. 14a, b, respectively. The absorption peak for 4-CP is observed at 288 nm. As evident from the figure, no change in the intensity was observed even after 20 min, thereby confirming that no degradation of 4-CP has taken place in dark due to surface adsorption phenomenon.

Figure 15a shows a plot of relative absorbance C/C_0 vs time for W_{NS}, W_{NR}, TiO_2 and without photocatalyst. No significant decrease was observed without photocatalyst. The maximum photocatalytic activity was shown by W_{NS} followed by W_{NR} and then TiO_2. Figure 15b shows the photocatalytic degradation rate constant (k) of 0.04088 min^{-1} for
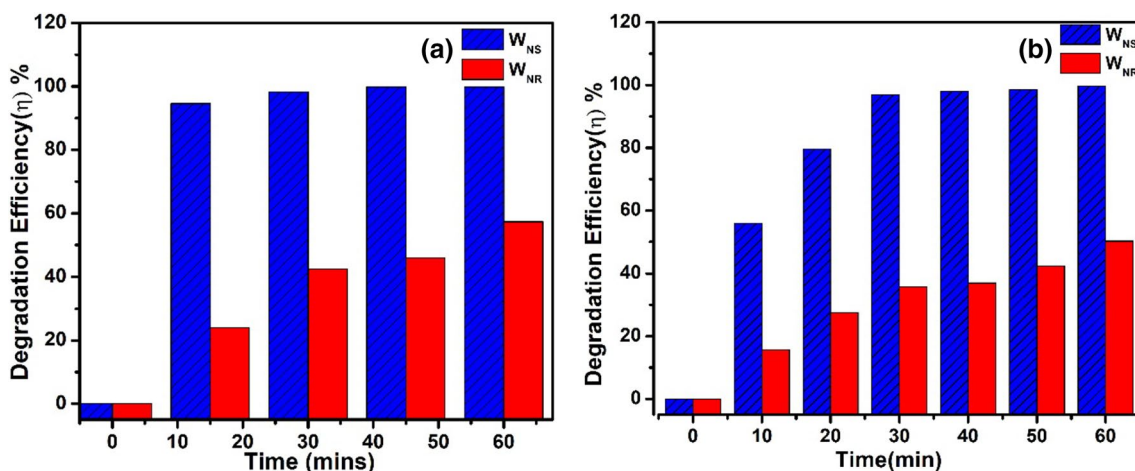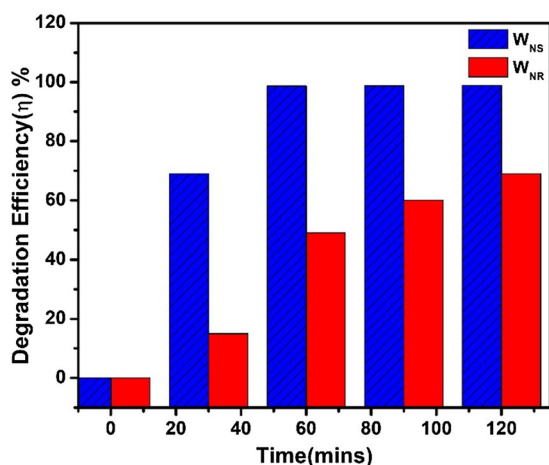

Fig. 13 Comparative degradation efficiency (η) % vs time plots of W_{NS} and W_{NR} on the photocatalytic degradation of MB using **a** 50 mg and **b** 20 mg of photocatalyst
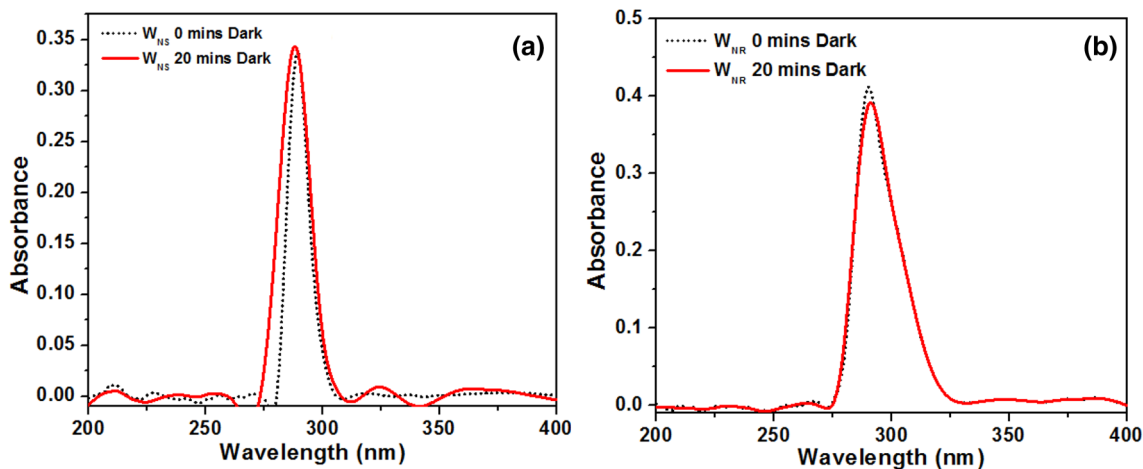
Fig. 14 4-CP dark reaction using **a** W_{NS} and **b** W_{NR}
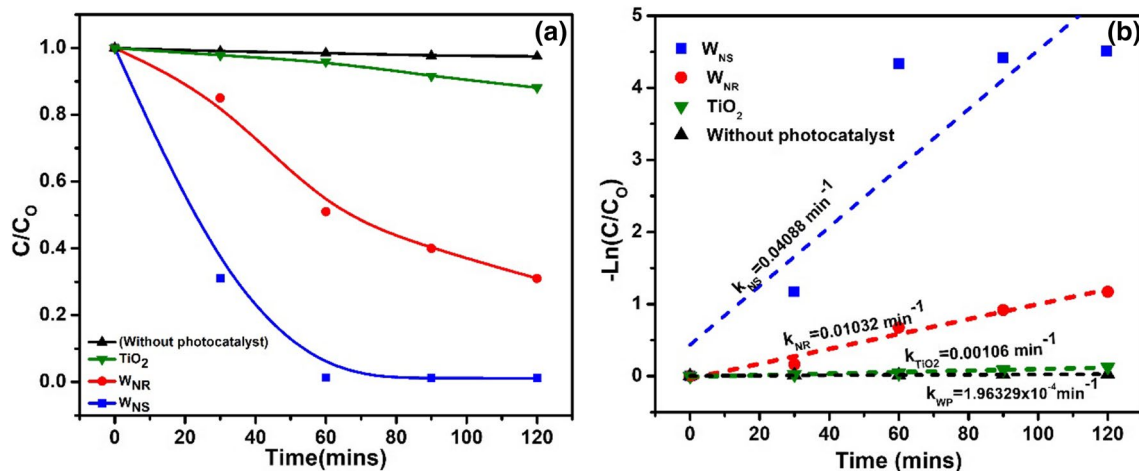
Fig. 15 Photodegradation studies of 4-CP by W_{NS}, W_{NR}, TiO_2 and without using photocatalyst: **a** C/C_0 vs time plot and **b** $-\ln(C/C_0)$ vs time plot

Fig. 16 Comparative degradation efficiency (η) % vs time plot for 4-CP using 50 mg of W_{NS} and W_{NR}

W_{NS}, 0.01038 min^{-1} for W_{NR}, 0.00106 min^{-1} for TiO_2 and 0.00002 min^{-1} without using photocatalyst.

Figure 16 shows the degradation efficiency of 4-CP at times $t = 30$, 60, 90 and 120 min for W_{NS} as 69%, 98.6%, 98.7% and 99.8% whereas for W_{NR} the efficiencies obtained are 15%, 49%, 60% and 69%, respectively. Thus, from the above data it can be concluded that W_{NS} has a higher photocatalytic degradation efficiency and rate as compared to W_{NR}.
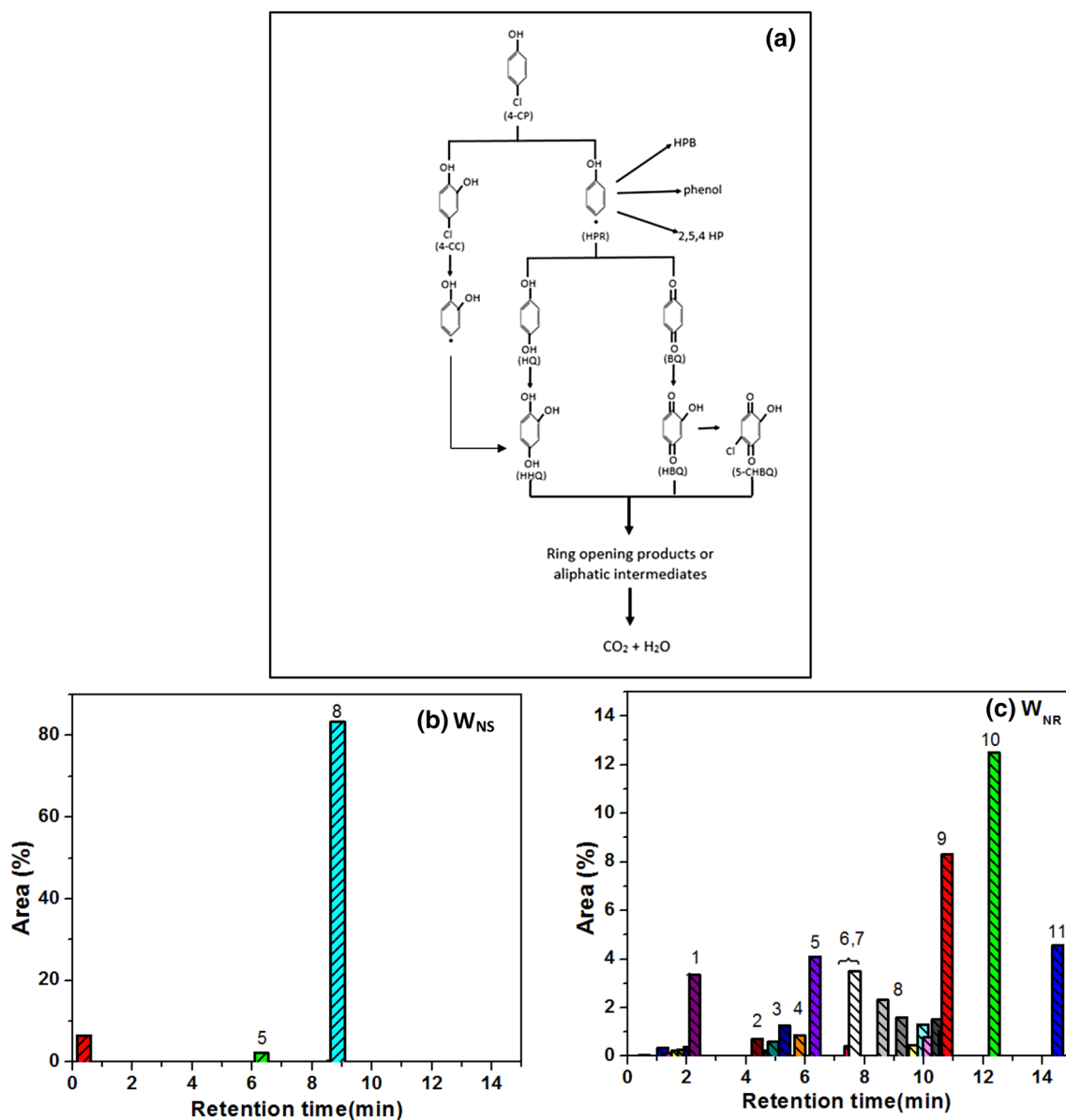
HPLC

HPLC studies were carried out for the determination of intermediate products during photocatalytic degradation of 4-CP as shown in Fig. 17. The primary degradation products of 4-CP are hydroquinone (HQ) and 4-chlorocatechol (4-CC). The attack of the hydroxyl radical on the ortho position results in the elimination of a hydrogen ion that leads to the formation of 4-CC while an attack on the para position leads to the formation of HQ. HPR (hydroxyl phenyl radical) resulting from hemolytic cleavage can form phenol and bi-cyclic compounds such as hydroxyphenyl (HP), benzoquinone (BQ) and 2,5,4-hydroxyphenyl (2,5,4-HP). Similarly, the reactive species (OH$^.$, O_2^-, HO_2^-) formed by the irradiation of the photocatalyst undergo reactions such as radical abstraction, elimination, and recombination with these compounds which result in the formation of other degradation products as shown in Fig. 17a (Rideh et al. 1997; Theurich et al. 1996; Li et al. 1999a, b).

Figure 17b, c shows HPLC plots (area vs characteristic retention time) of respective intermediate degradation products of 4-CP. For W_{NS}, two intermediates at retention times of 6.3 and 8.8 min were observed for W_{NS} which are ascribed to (HQ) and (4-CC). In W_{NR} HPLC chromatogram, intermediates were observed at retention times of 2.2, 4.3, 4.9, 5.8, 6.3, 7.5, 7.6, 9.2, 10.7, 12.3 and 14.5 min and were assigned to hydroxyhydroquinone (HHQ), hydroxybenzoquinone (HBQ), 2,5,4-hydroxyphenyl (2,5,4-HP), phenol, hydroquinone (HQ), benzoquinone (BQ), 4-hydroxyphenolbenzoquinone (4-HPB), 4-chlorocatechol (4-CC), 5-chlorobenzoquinone (5-CBQ), ring-opening product and 4-chlorophenol(4-CP).

It can be observed from the HPLC chromatogram of W_{NS} that 4-CP was completely degraded within 20 min as no peak of 4-CP was observed but small peak of 4-CP was observed in W_{NR} with other intermediates that proves that the degradation mechanism of W_{NS} is faster than that of W_{NR}. This can also be confirmed using the photocatalytic analysis of 4-CP degradation as shown earlier in Fig. 15. The

Fig. 17 HPLC study for the degradation of 4-CP **a** schematic of intermediate by-products of 4-CP and **b, c** HPLC plots (area vs retention time) of intermediates using W_{NS} and W_{NR}, respectively

study of photocatalytic degradation of MB by W_{NS} and W_{NR} also supports the above statement (Fig. 11). These studies provide evidence that W_{NS} and W_{NR} have proven to be a good photocatalyst for the degradation of dyes as well as organic pollutants (Table 3).

Mechanism of photocatalysis

WS_2 nanostructures were used as effective catalysts to study the photodegradation of MB and 4-CP. When the incoming photon has an energy greater than or equal to the band-gap (E_g) of WS_2 (Fig. 18), the valance band electron (e^-) is promoted to the conduction band which leaves behind a

hole (h^+) to react with H_2O to form hydroxyl radical ($OH^.$) and H^+ ion as shown in the following equations (Song et al. 2018; Sharma et al. 2017a, b):

$$WS_2 + h\nu \rightarrow e^- + h^+ \tag{5}$$

$$H_2O + h^+ \rightarrow OH^. + H^+ \tag{6}$$

The efficiency of photocatalysis depends on the number of ($OH^.$) radicals formed as they are powerful oxidizing agents and play a crucial role in the degradation of toxic dyes and pollutants. Another factor responsible for the degradation of dyes and pollutants is the formation of superoxide

Table 3 HPLC study of intermediates formed during photocatalytic degradation of 4-CP

Peak	Intermediate	Retention time (min)			References
		(W_{NS})	(W_{NR})	Reported	
1	Hydroxyhydroquinone (HHQ)		2.2	2.9	Theurich et al. (1996)
2	Hydroxybenzoquinone (HBQ)		4.3	3.7	Theurich et al. (1996)
3	2,5,4-Hydroxyphenyl (2,5,4-HP)		4.9	5.0	Theurich et al. (1996)
4	Phenol		5.8	6.1	Theurich et al. (1996)
5	Hydroquinone (HQ)	6.3	6.3	6.43	Rideh et al. (1997)
6	Benzoquinone (BQ)		7.5	6.9	Rideh et al. (1997)
7	4-Hydroxyphenylbenzoquinone (4-HPB)		7.6	7.5	Theurich et al. (1996)
8	4-Chlorocatechol (4-CC)	8.8	9.2	8.9	Theurich et al. (1996)
9	Ring-opening product		10.7	10.49	Li et al. (1999)
10	5-Chlorobenzoquinone (5-CBQ)		12.3	12.1	Li et al. (1999)
11	4-Chlorophenol (4-CP)		14.5	15.1	Theurich et al. (1996)
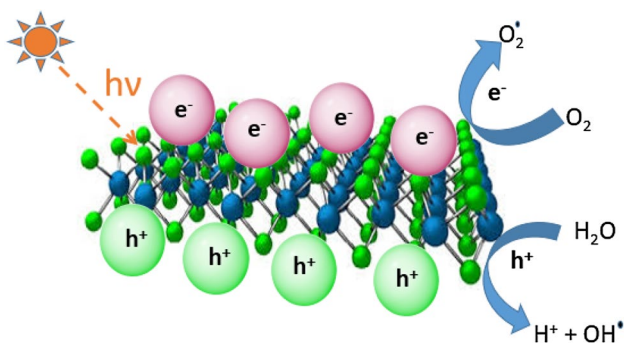
Fig. 18 Mechanism of photocatalytic degradation

anions (O_2^-) which are formed when the electrons in the valence band are accepted by oxygen molecules adsorbed on the photcatalyst surface as shown in the following equation (Sharma et al. 2016):

$$O_2 + e^- \rightarrow O_2^- \qquad (7)$$

The superoxide anion radical then loses its electron to the holes present in the valence band to form superoxide anion radical ($O_2^.$). The hydroxyl radical (OH$^.$) and superoxide anion radical ($O_2^.$) together form the reactive oxygen species (ROS) and react along with H^+ ions to form H_2O_2 (Eqs. (6), (7)) reactive species which proceed with the photodegradation of toxic dyes and organic pollutants and lead to the formation of harmless by-products (Singh et al. 2018):

$$O_2^. + 2H^+ \rightarrow H_2O_2 \qquad (8)$$

$$H_2O_2 + e^- \rightarrow OH^. + OH^- \qquad (9)$$

Photocatalysis is enhanced when the time of separation between electrons and holes increases thereby causing a hinderance to the recombination process. The photocatalytic mechanism depends on the separation of reactive species to form radicals that are used in the degradation of pollutant.

Thus, recombination of holes and electrons due to defects causes a slower photocatalytic degradation of pollutants as observed in the case of W_{NR}, due to high defect density which was confirmed from PL and Raman studies. A higher intensity means less number of defects in the case of W_{NS} thereby causing it to have a faster photocatalytic degradation mechanism. This phenomenon is also confirmed by the higher pore size of W_{NS} as observed in BET analysis, thus responsible for a slower recombination process and higher intensity of W_{NS} in the PL spectra suggesting a lesser number of defects that cause faster photodegradation due to delayed recombination as discussed earlier in BET and PL analysis.

Conclusion

A systematic study was conducted to compare the morphology-dependent photocatalytic activity of the WS$_2$ nanostructures, WS$_2$ nanosheets (W_{NS}) and WS$_2$ nanorods (W_{NR}), synthesized by the hydrothermal technique. Photocatalytic degradation efficiency (η) and rate kinetics (k) of MB [(η ~ 100% with $k_{NS} = 0.1077$ min^{-1} by W_{NS}) and (η ~ 50% with $k_{NR} = 0.01364$ by W_{NR})] in 60 min and for 4-chlorophenol [(η ~ 100% with $k_{NS} = 0.04088$ min^{-1} by W_{NS}) and (η ~ 69% with $k_{NR} = 0.01038$ min^{-1} by W_{NR})] in 120 min were observed. Comparative HPLC studies in W_{NS} and W_{NR} samples were also carried out to determine the intermediate degradation products of 4-CP. The increased degradation efficiency of W_{NS} over W_{NR} is attributed to (1) large pore size (as evident through BET analysis) and (2) reduced number of defects (as observed in PL and Raman studies) of W_{NS} as compared to W_{NR}.

Compliance with ethical standards

Conflict of interest There are no conflicts of interest to declare.

References

Aslam M, Soomro TM, Ismail IMI, Salah N, Gondal MA, Hameed A (2015) Sunlight mediated removal of chlorophenols over tungsten supported ZnO: electrochemical and photocatalytic studies. J Environ Chem Eng 707:1–11. https://doi.org/10.1016/j.jece.2015.07.004

Baral A, Khanuja M, Islam SS, Sharma R, Mehta BR (2017) Identification and origin of visible transitions in one dimensional (1d) ZnO nanostructures: excitation wavelength and morphology dependence study. J Lumin 183:383–390. https://doi.org/10.1016/j.jlumin.2016.11.060

Bhuyan T, Mishra K, Khanuja M, Prasad R, Varma A (2015a) Biosynthesis of zinc oxide nanoparticles from *Azadirachta indica* for antibacterial and photocatalytic applications. Mater Sci Semicond Process 32:55–61. https://doi.org/10.1016/j.mssp.2014.12.053

Bhuyan T, Khanuja M, Sharma R, Patel S, Reddy MR, Anand S, Varma A (2015b) A comparative study of pure and copper (Cu)-doped ZnO nanorods for antibacterial and photocatalytic applications with their mechanism of action. J Nanoparticle Res 17:288. https://doi.org/10.1007/s11051-015-3093-3

Cao S, Liu T, Hussain S, Zeng W, Peng X (2014) Hydrothermal synthesis of variety low dimensional of WS$_2$ nanostructures. Materials Lett 129:205–208. https://doi.org/10.1016/j.matlet.2014.05.01

Cao S, Liu T, Hussain S, Zeng W, Peng X (2015) Hydrothermal synthesis and controlled growth of tungsten disulphide nanostructures from one dimension to three dimension. Micro Nano Lett 10:183–186. https://doi.org/10.1049/mnl.2014.0516

Chaudhary N, Khanuja M, Islam SS (2018) Hydrothermal synthesis of MoS$_2$ nanosheets for multiple wavelength optical sensing applications. Sens Actuators A Phys 277:190–198. https://doi.org/10.1016/j.sna.2018.05.008

Ghorai A, Midya A, Maiti R, Ray SK (2016) Exfoliation of WS$_2$ in the semiconducting phase using a group of lithium halides: a new method of Li intercalation. Dalton Trans 45:14979–14987. https://doi.org/10.1039/c6dt02823c

Ghorai A, Bayan S, Gogurla N, Midya A, Ray SK (2017) Highly luminescent WS$_2$ quantum dots/ZnO heterojunctions for light emitting devices. ACS Appl Mater Interfaces 9:558–565. https://doi.org/10.1021/acsami.6b12859

Goldman EB, kartvelishvily E, Zaidman SL, Cohen RS, Palmon A, Hovav AH, Aframian DJ, Zak A, Tenne R, Neumann Y (2015) Biocompatibility of tungsten disulfide inorganic nanotubes and fullerene-like nanoparticles with salivary glands. Tissue Eng 21:1013–1023. https://doi.org/10.1089/ten.tea.2014.0163

Guo L, Sun H, Dai D, Cui J, Li M, Xu Y, Xu M, Du Y, Jiang N, Huang F, Lin CT (2018) Direct formation of wafer-scale single-layer graphene films on the rough surface substrate by PECVD. Carbon 129:456–461. https://doi.org/10.1016/j.carbon.2017.12.023

He K, Zhao C, Zhao G, Han G (2015) Effects of pore size on the photocatalytic activity of mesoporous TiO$_2$ prepared by a sol–gel process. J Sol Gel Sci Technol 75:557–563. https://doi.org/10.1007/s10971-015-3726-0

Jiang X, Sun B, Song Y, Dou M, Ji J, Wang (2017) One-pot synthesis of MoS$_2$/WS$_2$ ultrathin nanoflakes with vertically aligned structure

on indium tin oxide as a photocathode for enhanced photo-assistant electrochemical hydrogen evolution reaction. RSC Adv 7:49309–49319. https://doi.org/10.1039/C7RA10762E

Kartal N, Sökmen M (2011) New catalyst systems for the degradation of chlorophenols. Desalination 281:209–214. https://doi.org/10.1016/j.desal.2011.07.066

Khodaie M, Ghasemi N, Moradi B, Rahimi M (2013) Removal of methylene blue from wastewater by adsorption onto ZnCl$_2$ activated corn husk carbon equilibrium studies. J chem 2013:1–6. https://doi.org/10.1155/2013/383985

Leofanti G, Padovan M, Tozzola G (1998) Surface area and pore texture of catalysis. Catal Today 41:207–219. https://doi.org/10.1016/S0920-5861(98)00050-9

Li X, Cubbage JW, Jenks WS (1999a) Photocatalytic degradation of 4-chlorophenol. 2. The 4-chlorocatechol pathway. J Org Chem 37:8525–8536. https://doi.org/10.1021/jo990912n

Li X, Cubbage JW, Tetzlaff TA, Jenks WS (1999b) Photocatalytic degradation of 4-chlorophenol. 1. The hydroquinone pathway. J Org Chem 29:8509–8524. https://doi.org/10.1021/jo990820y

Liu Y, Liu J (2017) Hybrid nanomaterials of WS$_2$ or MoS$_2$ nanosheets with liposomes: biointerfaces and multiplexed drug delivery. Nanoscale 35:12759–13346. https://doi.org/10.1039/C7NR04199C

Moonsiri M, Rangsunvigit P, Chavadej S, Gulari E (2004) Effects of Pt and Ag on the photocatalytic degradation of 4-chlorophenol and its by-products. Chem Eng J 97:241–248. https://doi.org/10.1016/j.cej.2003.05.003

Narang J, Singhal C, Khanuja M, Mathur A, Jain A, Pundir CS (2017) Hydrothermally synthesized zinc oxide nanorods incorporated on lab-on-paper device for electrochemical detection of recreational drug. Artif Cells Nanomed Biotechnol 46:1586–1593. https://doi.org/10.1080/21691401.2017.1381614

Narang J, Mishra A, Pilloton R, Alekhya V, Wadhwa S, Pundir CS, Khanuja M (2018) Development of MoSe$_2$ nano-urchins as a sensing platform for a selective bio-capturing of *Escherichia coli* shiga toxin DNA. Biosensors 8(3):77. https://doi.org/10.3390/bios8030077

Navale Govinda R, Sekhar RC, Gohil Kushal N, Dharne Mahesh S, Late Dattatray J, Shinde Sandip S (2015) Oxidative and membrane stress-mediated antibacterial activity of WS2 and rGO-WS2 nanosheets. RSC Adv 5:74726–74733. https://doi.org/10.1039/C5RA15652A

Nguyen AT, Juang RS (2015) Photocatalytic degradation of p-chlorophenol by hybrid H$_2$O$_2$ and TiO$_2$ in aqueous suspensions under UV irradiation. J Environ Manage 147:271–277. https://doi.org/10.1016/j.jenvman.2014.08.023

Peng W, Li Y, Zhang F, Zhang G, Fan X (2017) Roles of two-dimensional transition metal dichalcogenides as cocatalysts in photocatalytic hydrogen evolution and environmental remediation. Ind Eng Chem Res 56:4611–4626. https://doi.org/10.1021/acs.iecr.7b00371

Piao M, Chu J, Wang X, Chi Y, Zhang H, Li C, Shi H, Joo MK (2018) Hydrothermal synthesis of stable metallic 1T phase WS2 nanosheets for thermoelectric application. Nanotechnology 29(2):02570. https://doi.org/10.1088/1361-6528/aa9bfe

Rideh L, Wehrer A, Ronze D, Zoulalian A (1997) Photocatalytic degradation of 2-chlorophenol in TiO2 aqueous suspension: modeling of reaction rate. Ind Eng Chem Res 36(11):4712–4718. https://doi.org/10.1021/ie970100m

Sade H, Lellouche JP (2018) Preparation and characterization of WS$_2$@SiO$_2$ and WS$_2$@PANI core-shell nanocomposites. Nanomat 8:156. https://doi.org/10.3390/nano8030156

Sang Y, Zhao Z, Zhao M, Hao P, Leng P, Liu H (2014) From UV to near-infrared, WS$_2$ nanosheet: a novel photocatalyst for full solar light spectrum photodegradation. Adv mater 27:363–369. https://doi.org/10.1002/adma.201403264

Sharma R, Singh S, Varma A, Khanuja M (2016) Visible light induced bactericidal and photocatalytic activity of hydrothermally synthesized BiVO$_4$ nano-octahedrals. J Photochem Photobiol 162:266–272. https://doi.org/10.1016/j.jphotobiol.2016.06.035

Sharma R, Khanuja M, Islam SS, Varma A (2017a) Aspect-ratio-dependent photoinduced antimicrobial and photocatalytic organic pollutant degradation efficiency of ZnO nanorods. Res Chem Intermed 43:5345–5364. https://doi.org/10.1007/s11164-017-2930-7

Sharma R, Khanuja M, Sinha OP, Narayan SN (2017b) Reduced band gap and charge recombination rate in Se doped α-Bi$_2$O$_3$ leads to enhance photoelectrochemical and photocatalytic performance: theoretical and experimental insight. Int J Hydrog Energy 42:20638–20648. https://doi.org/10.1016/j.ijhydene.2017.07.011

Shi W, Lin ML, Tan QH, Qiao XF (2016) Raman and photoluminescence spectra of two-dimensional nanocrystallites of monolayer WS$_2$ and WSe$_2$. 2D Materials 3:025016. https://doi.org/10.1088/2053-1583/3/2/025016

Siddiqui I, Mittal H, Kohli VK, Gautam P, Ali M, Khanuja M (2018) Hydrothermally synthesized micron sized, broom-shaped MoSe$_2$ nanostructures for superior photocatalytic water purification. Mat Res Exp 5:12. https://doi.org/10.1088/2053-1591/aae241

Singh S, Pendurthi R, Khanuja M, Suchitra R, Islam SS, Shivaprasad SM (2017a) Copper-doped modified ZnO nanorods to tailor its light assisted charge transfer reactions exploited for photo-electrochemical and photo-catalytic application in environmental remediation. Appl Phys A 123:184. https://doi.org/10.1007/s00339-017-0806-8

Singh S, Ruhela A, Rani S, Khanuja M, Sharma R (2017b) Concentration specific and tunable photoresponse of bismuth vanadate functionalized hexagonal ZnO nanocrystals based photoanodes for photoelectrochemical application. Solid State Sci 76:48–56. https://doi.org/10.1016/j.solidstatesciences.2017.12.003

Singh S, Sharma R, Khanuja M (2018) A review and recent developments on strategies to improve the photocatalytic elimination of organic dye pollutants by BiOX (X = Cl, Br, I, F) nanostructures. Korean J Chem Eng 35:1955–1968. https://doi.org/10.1007/s11814-018-0112-y

Singhal C, Khanuja M, Chaudhary N, Pundir CS, Narang J (2018) Detection of chikungunya virus DNA using two-dimensional MoS$_2$ nanosheets based disposable biosensor. Sci Rep 8:7734. https://doi.org/10.1038/s41598-018-25824-8

Song W, Xiao P, Lou J (2018) Enhanced visible light driven photocatalysis from WS$_2$ quantum dots coupled with BiOCl nanosheets: synergistic effect and mechanism insight. Catal Sci Tech 8:201–209. https://doi.org/10.1039/C7CY01784G

Tang G, Tang H, Li C, Li W, Ji X (2011) Surfactant-assisted hydrothermal synthesis and characterization of WS$_2$ nanorods. Mater Lett 65:3457–3460. https://doi.org/10.1016/j.matlet.2011.07.033

Theurich J, Lindner M, Bahnemann DW (1996) Photocatalytic degradation of 4-chlorophenol in aerated aqueous titanium dioxide suspensions: a kinetic and mechanistic study. Langmuir 12:6368–6376. https://doi.org/10.1021/la960228t

Vattikuti SVP, Byon C, Reddy CV (2016a) Preparation and improved photocatalytic activity of mesoporous WS$_2$ using combined hydrothermal-evaporation induced self assembly. Mater Res Bull 95:193–203. https://doi.org/10.1016/j.materresbull.2015.11.059

Vattikuti SVP, Byon C, Chitturi V (2016b) Selective hydrothermally synthesis of hexagonal WS$_2$ platelets and their photocatalytic performance under visible light irradiation. Superlattices Microstruct 94:39–50. https://doi.org/10.1016/j.spmi.2016.03.042

Wang B, Zhang Z, Chang K, Cui J, Rosenkranz A, Yu J, Lin CT, Chen G, Zang K, Luo J, Jiang N, Guo D (2018) New deformation-induced nanostructure in silicon. Nano Lett 18:4611–4617. https://doi.org/10.1021/acs.nanolett.8b01910

Wu Y, Liu Z, Chen J, Cai X, Na P (2017) Hydrothermal fabrication of hyacinth flower-like WS$_2$ nanorods and their photocatalytic properties. Mater Lett 189:282–285. https://doi.org/10.1016/j.matlet.2016.11.024

Yu ZZ, Xia HY, Ming GD (2013) A model for nanogrinding based on direct evidence of groundchips of silicon wafer. Sci China Technol 56:2099–2108. https://doi.org/10.1007/s11431-013-5286-2

Yue B, Zhou Y, Xu J, Wu Z, Zhang X, Zou Y, Jin S (2002) Photocatalytic degradation of aqueous 4 chlorophenol by silica-immobilized polyoxometalates. Environ Sci Technol 36:1325–1329. https://doi.org/10.1021/es011038u

Zhang Z, Huo F, Zhang X, Guo D (2012) Fabrication and size prediction of crystalline nanoparticles of silicon induced by nanogrinding with ultrafine diamond grits. Scr Mater 67:657–660. https://doi.org/10.1016/j.scriptamat.2012.07.016

Zhang Z, Guo D, Wang B, Kang R, Zhang B (2015a) A novel approach of high speed scratching on silicon wafers at nanoscale depths of cut. Sci Rep 5:16395. https://doi.org/10.1038/srep16395

Zhang Z, Wang B, Kang R, Zhang B, Guo D (2015b) Changes in surface layer of silicon wafers from diamond scratching. CIRP Ann 64:349–352. https://doi.org/10.1016/j.cirp.2015.04.005

Zhang X, Xu H, Wang J, Ye X, Lei W, Xue M, Tang H, Li C (2016a) Synthesis of ultrathin WS$_2$ nanosheets and their tribological properties as lubricant additives. Nanoscale Res Lett 11:442. https://doi.org/10.1186/s11671-016-1659-3

Zhang Z, Wang B, Huang S, Wen B, Yang S, Zhang B, Lin CT, Jiang N, Jin Z, Guo D (2016b) A novel approach to fabricating a nano twinned surface on a ternary nickel alloy. Materials Des 106:313–320. https://doi.org/10.1016/j.matdes.2016.06.004

Zhang Z, Du Y, Wang B, Wang Z, Kang R, Guo D (2017a) Nanoscale wear layers on silicon wafers Induced by mechanical chemical grinding. Tribol Lett 65:132. https://doi.org/10.1007/s11249-017-0911-z

Zhang Z, Cui J, Wang B, Wang Z, Kang R, Guo D (2017b) A novel approach of mechanical chemical grinding. J Alloys Compd 726:514:524. https://doi.org/10.1016/j.jallcom.2017.08.024

Zhang Z, Huang S, Wang S, Wang B, Bai Q, Zhang B, Kang R, Guo D (2017c) A novel approach of high-performance grinding using developed diamond wheels. Int J Adv Manuf Technol 91:3315–3326. https://doi.org/10.1007/s00170-017-0037-3

Zhang Z, Cui J, Wang B, Jiang H, Chen G, Yu J, Lin C, Tang C, Hartmaier A, Zhang J, Luo J, Rosenkranz A, Jiang N (2018) In situ TEM observation of rebonding on fractured silicon carbide. Nanoscale 10:6261–6269. https://doi.org/10.1039/c8nr00341f

مدينة الملك عبدالعزيز
KACST للعلوم والتقنية

Springer